Destructive Little-Parks Effect in a Full-Shell Nanowire-Based Transmon

Sabonis, Deividas; Erlandsson, Oscar; Kringhøj, Anders; Van Heck, Bernard; Larsen, Thorvald W.;
Petkovic, Ivana; Krogstrup, Peter; Petersson, Karl D.; Marcus, Charles M.

Important note
To cite this publication, please use the final published version (if applicable).
Please check the document version above.

Destructive Little-Parks Effect in a Full-Shell Nanowire-Based Transmon

Deividas Sabonis[1,2,*] Oscar Erlandsson[1,2,*] Anders Kringhøj[1,2,*] Bernard van Heck,[3] Thorvald W. Larsen[1,2]
Ivana Petkovic,[1,2] Peter Krogstrup,[1,4] Karl D. Petersson[1,2] and Charles M. Marcus[1,2]

[1]*Center for Quantum Devices, Niels Bohr Institute, University of Copenhagen, 2100 Copenhagen, Denmark*
[2]*Microsoft Quantum Lab–Copenhagen, Niels Bohr Institute, University of Copenhagen, 2100 Copenhagen, Denmark*
[3]*Microsoft Quantum Lab Delft, Delft University of Technology, 2600 GA Delft, Netherlands*
[4]*Microsoft Quantum Materials Lab–Copenhagen, 2800 Lyngby, Denmark*

A semiconductor transmon with an epitaxial Al shell fully surrounding an InAs nanowire core is investigated in the low E_J/E_C regime. Little-Parks oscillations as a function of flux along the hybrid wire axis are destructive, creating lobes of reentrant superconductivity separated by a metallic state at a half quantum of applied flux. In the first lobe, phase winding around the shell can induce topological superconductivity in the core. Coherent qubit operation is observed in both the zeroth and first lobes. Splitting of parity bands by coherent single-electron coupling across the junction is not resolved beyond line broadening, placing a bound on Majorana coupling, $E_M/h < 10$ MHz, much smaller than the Josephson coupling $E_J/h \sim 4.7$ GHz.

Variants of the conventional metallic transmon qubit [1,2] based on a semiconductor nanowires (NWs) with an epitaxial superconducting shell have appeared recently and shown great promise for qubit applications, offering atomically precise interfaces and electrostatic control of junction properties [3–7]. By now, qubit spectroscopy [3], coherence [4], two-qubit operation [5], gate-controlled qubit coupling [8], and dc monitoring [9] have been demonstrated, along with investigations of applied magnetic field [7], junction Andreev bound states [6,10], anharmonicity [11], charge dispersion [12,13], spin [14], and parity protection [15]. However, axial flux effects from a fully surrounding Al shell on Josephson coupling have not been considered previously. This is more than a detail. In these small-diameter systems, it is known that an axial magnetic field applied to a cylindrical superconducting shell can give rise to an extreme form of the Little-Parks effect [16] characterized by flux-driven reentrant superconductivity [17–19], and, in semiconductor-superconductor hybrids to a possibility to realize topological superconductivity [20].

Proposals to realize transmons based on topological superconductors typically require sizeable applied magnetic fields to drive the system into the topological phase [21–25]. In these schemes, a properly oriented magnetic field splits the spin-orbit band, typically requiring ∼1 T to reach the topological regime [26], a challenge to most superconducting technologies [7] with some exceptions [27]. Recent experiments and theory indicate that topological superconductivity can be induced in a NW with a fully surrounding superconducting shell by winding the superconducting phase around the wire using magnetic flux

rather than Zeeman coupling, requiring lower fields (∼0.1 T) to reach the first reentrant superconducting lobe in the destructive Little-Parks effect regime [20].

In an ideal topological transmon, a pair of Majorana zero modes (MZMs) straddle the Josephson junction, and are coupled via coherent single-electron tunneling with a characteristic energy scale E_M, which accompanies the usual Josephson coupling, E_J, across the junction [23,28,29]. From the perspective of circuit quantum electrodynamics spectroscopy, E_M splits the parity-preserving level crossings thereby doubling the number of spectral lines [23]. The prediction of E_M from device parameters is difficult as E_M depends sensitively on the potential in the junction. While E_M is expected to increase as the junction barrier is lowered, its value is likely limited by the presence of additional transport channels within the subgap spectrum of the junction [25,30].

In this Letter, we investigate InAs/Al hybrid semiconductor-based NWs with a fully surrounding superconducting shell, comparing qubit spectra and coherence in the zeroth (trivial) lobe to the first reentrant lobe, corresponding to roughly one flux quantum ($\Phi_0 = h/2e$) of applied magnetic field through the Al shell, where topological superconductivity is anticipated. We focus on the offset-charge-sensitive transmon regime [31–34] to facilitate a direct examination of the parity of the superconducting island. Coherence was observed via spectral and time-domain measurements in both the zeroth and first superconducting lobes. The destructive Little-Parks effect causes a field-dependent superconducting gap, and the destruction of superconductivity altogether between lobes, around an applied flux of $\Phi_0/2$. We model the effects of
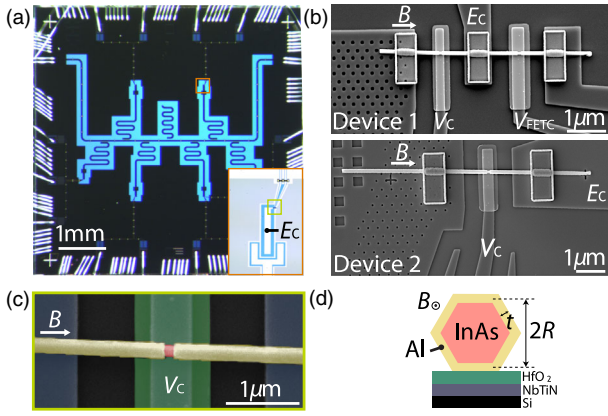
FIG. 1. (a) Optical micrograph of the sample chip showing multiple separate qubit readout resonators connected to a single readout line. The inset shows an enlargement of a sample area and a transmon island capacitor with a charging energy E_C. (b) Scanning electron micrographs of two investigated devices: top—device 1, bottom—device 2. Gate voltage V_C in both devices controlled both qubit frequency (large range) and offset charge (small range). Device 1 was decoupled from dc lead (right side) with negative V_{FETC}. The capacitor island is connected in the middle of device 1 and on right side in device 2. (c) False colored enlargment of the semiconductor junction (red) in device 2 where Al shell (yellow) is removed, controlled by gate below the dielectric (green). (d) Schematic cross section of the hybrid nanowire and substrate stack, showing mean diameter, $2R$, shell thickness, t and direction of applied field B.

flux on qubit frequency, finding good agreement with experiment. We do not observe clear splittings of gate-modulated charge dispersion bands. Such splitting would reflect coherent Majorana coupling anticrossing the parity bands. This allows us to set a bound on Majorana coupling across the semiconductor junction, $E_M/h < 10$ MHz.

A chip containing six NW hybrid transmons and individual readout resonators is shown in Fig. 1(a). The circuit ground plane, qubit island, and all control and readout elements (electrostatic gates, on-chip gate filters, readout resonator, transmission line, and NbTiN crossovers on all control lines) were fabricated from sputtered NbTiN, patterned using e-beam lithography and reactive ion etching on a high-resistivity silicon wafer. The charging energy of the qubit island $E_C/h = 512$ MHz was estimated from electrostatic simulations. The experimental determination of E_C/h in SNS transmons is nontrivial due to gate-voltage dependent number of channels and their individual transmissions.

The inset in Fig. 1(a) shows an enlargement of a sample area and a transmon island capacitor. The NW is approximately 10 μm long and resides on top of a HfO_2 dielectric that separates it from the bottom gates. Eight working devices were measured and showed similar results. We present data from two representative devices (device 1 and device 2) shown in Fig. 1(b). For device 1, one side of the NW is connected to ground plane and the other makes an

ohmic contact with NbTiN, allowing dc monitoring that can be connected and disconnected *in situ* [9] using gate voltage V_{FETC}. The contact in the middle of the NW connects the junction to the qubit island. Device 2 is a simpler design, with one side of the NW connected to the qubit island and the other to the ground plane. All measurements are performed in a BlueFors XLD dilution refrigerator with a base temperature of 20 mK and $1 - 1 - 6$ vector magnet.

Figure 1(c) shows an enlargement (device 2) of the gate-controlled Josephson junction in the full-shell NW. The junction was formed by wet etching the Al shell in a 100–150 nm region defined by electron-beam lithography. The voltage V_C on the bottom gate was used to tune the junction coupling. The same gate was used to tune both the qubit frequency, on a large voltage range, and the offset charge, on a small voltage range. The schematics of the cross section of the full-shell InAs/Al NW together with a substrate material stack is shown in Fig. 1(d).

Measurements were performed using two-tone spectroscopy, where a microwave drive pulse is followed by a readout tone close to the cavity frequency. After the readout tone enters the readout cavity, it interacts with the respective resonator before being amplified by a traveling wave parametric amplifier at base temperature, high electron mobility transistor amplifier at 4 K, and additional amplification at room temperature. The signal is then mixed to an intermediate frequency and sampled followed by digital heterodyne detection to extract the cavity response, V_H.

As a first signature of the Little-Parks lobe structure, we examine qubit frequency as a function of axial magnetic field, B. The zero-field qubit frequency was set to $\sim$4.3 GHz ($V_C \sim -2.5$ V) slightly below the readout resonator frequency, $f_r \sim 5.29$ GHz for device 1. A map of the amplitude of the heterodyne demodulated transmission V_H (line average subtracted) as a function of qubit drive frequency f_d and magnetic field B is shown in Fig. 2(a). At each field step the readout frequency was adjusted by tracking the frequency of the resonator. At low fields, $B \lesssim 40$ mT, the NW is in the zeroth lobe, with a trivial proximity effect from the shell, and a field dependent gap, $\Delta(B)$ with its maximum value, Δ_0 at $B = 0$. At intermediate fields, around $\sim$50 mT, the qubit frequency falls rapidly, the resonance broadens and disappears. This behavior is associated with the destructive regime around applied flux $\Phi_0/2$, where $\Delta(B)$ goes to zero and superconductivity is destroyed [19,20]. At higher fields, $B \sim 60$–120 mT the qubit is recovered and shows similar behavior to the low-field regime with a maximum qubit frequency around 90 mT, slightly reduced from its zero-field value. This recovery of qubit frequency reflects the underlying lobe structure of superconductivity in the NW [19]. In the first lobe, one vortex has entered the shell, the superconducting phase twists once around the wire
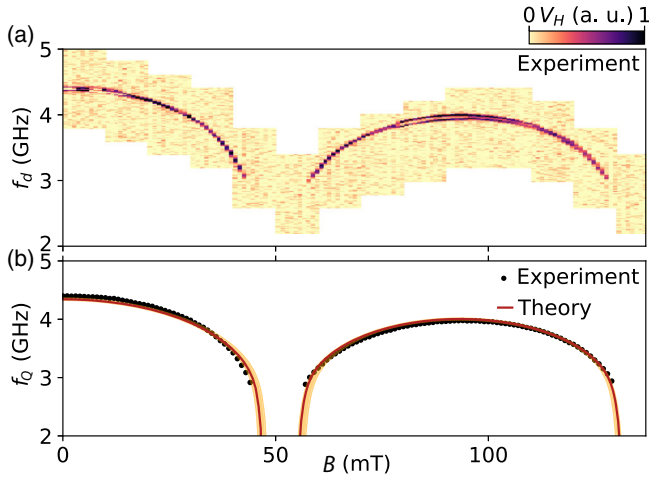
FIG. 2. (a) Two-dimensional map of two-tone spectroscopy as a function of drive frequency (f_d) and parallel magnetic field B for device 1. Four regimes are seen: (i) low fields (0–40 mT), zeroth superconducting lobe, qubit frequency f_Q decreases with increasing B; (ii) destructive regime, around half flux quantum $\Phi_0/2 \sim 50$ mT, qubit coherence is lost; (iii) higher fields (60–120 mT), first lobe, coherence is recovered with slightly reduced f_Q; and (iv) second destructive regime at $\sim$135 mT where coherence is again lost. (b) Experiment (black points) and theory (orange curve) for qubit frequency, f_Q. Width of theory curve marks 3rd and 97th percentiles of the fit.

circumference, and topological superconductivity can be realized in the core [20].

We model the field dependence of the qubit frequency by considering a cylindrical shell of radius R and thickness t in an axial magnetic field B. Following Refs. [18,19,35], the pair-breaking term $\alpha(B)$ is calculated as

$$\alpha(B) = \frac{4\xi^2 k_B T_{C0}}{\pi R^2}\left[\left(n - \frac{\Phi}{\Phi_0}\right)^2 + \frac{t^2}{4R^2}\left(\frac{\Phi^2}{\Phi_0^2} + \frac{n^2}{3}\right)\right], \quad (1)$$

where ξ is the zero-field coherence length, T_{C0} is the zero field critical temperature and $\Phi = \pi R^2 B$ is the applied magnetic flux. The winding number n which is energetically favourable is determined by minimizing α versus n at a given magnetic field B. Once $\alpha(B)$ is known, the field dependence of the pairing energy $\Delta(B)$ can be determined numerically [36] based on Larkin's theory for cylindrical superconductors in a magnetic field [37].

We relate the field dependent gap $\Delta(B)$ to qubit frequency f_Q assuming the proportionality $E_J(B) \propto \Delta(B)$ and taking $E_J \gg E_C$, which yields a scaling relation $f_Q = f_0 d(B)^{1/2}$ where $d(B) = \Delta(B)/\Delta_0$. A numerical fit was then used to determine the four fit parameters, $R = 81$ nm, $t = 36$ nm, $\xi = 139$ nm, and $f_0 = 4.34$ GHz, yielding the theory curve in Fig. 2(b), which is in good agreement with experiment. The extracted geometrical fit parameters t and R are comparable to the values estimated from the electron micrograph in Fig. 1(b).

Details of the fitting procedure are given in an accompanying analysis notebook [38].

Time-domain measurements in the zeroth and first lobes are compared in Fig. 3. In the zeroth lobe ($B = 0$), Rabi oscillations with qubit drive frequency f_d set to match $f_Q = 4.53$ GHz were measured [Fig. 3(a)]. Data (black points) are shown together with the best fit to an exponentially decaying sinusoidal oscillation, $A \exp(-\tau/T^R)\sin(\omega\tau + \phi) + C$ (orange) as a function of pulse duration τ (with T_R, ω, ϕ, C, and A as fit parameters) and yields a Rabi decay time of $T^R = 0.18$ μs. Qubit lifetime in the zeroth lobe was measured by exciting the qubit using the π pulse, the length of which is found from Fig. 3(a), and measuring the qubit response after a time τ, yielding $T_1 = 2.5$ μs. In the first lobe ($B = 100$ mT), the Rabi decay time $T^R = 0.34$ μs was measured with relaxation time $T_1 = 0.5$ μs at $f_Q = 3.75$ GHz, which is somewhat shorter than in the zeroth lobe, which could be attributed to dissipation from subgap states present in the first lobe [20] (see the Supplemental Material [39]). We believe that the modest increase in Rabi decay time in the first lobe is related to unintentional detuning of the drive frequency in the zeroth lobe data [Fig. 3(a)]. Transport measurements were performed by setting V_{FETC} positive. Superconductor-insulator-superconductor spectroscopy in the first lobe showed no clear Majorana signatures, that is,
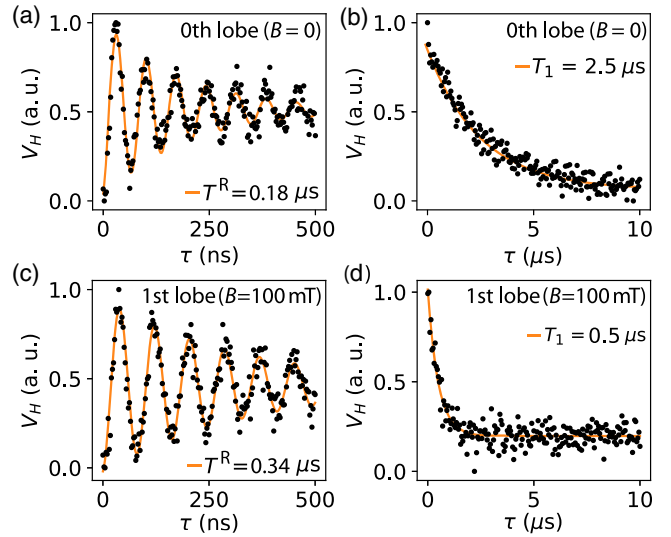

FIG. 3. (a) Rabi oscillations (black points) in the zeroth lobe ($B = 0$) in device 1 with best fit exponentially decaying sinusoidal oscillation, $A \exp(-\tau/T^R)\sin(\omega\tau + \phi) + C$ (orange) as a function of pulse duration τ, yields Rabi time $T^R = 0.18$ μs at qubit frequency $f_Q = 4.53$ GHz. (b) Qubit relaxation (black points) as a function of delay τ, with best fit to exponential decay, $A \exp(-\tau/T_1) + C$ (orange) yields $T_1 = 2.5$ μs. (c),(d) Same as (a),(b) except in the first lobe ($B = 100$ mT) yield Rabi and relaxation times, $T^R = 0.34$ μs and $T_1 = 0.5$ μs at qubit frequency $f_Q = 3.75$ GHz.
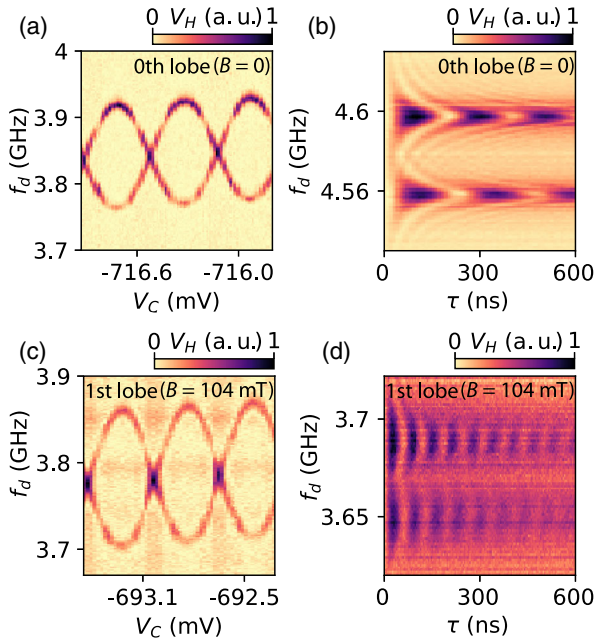
FIG. 4. (a) Qubit spectrum as a function of the gate voltage V_C in the zeroth lobe ($B = 0$) for device 2 showing two sinusoidal parity branches. The simultaneous appearance of both branches indicates that parity switching (poisoning) is faster than data acquisition time. (b) Coherent oscillations of both parity branches at slightly different V_C compared to (a) as a function of the drive time τ in the zeroth lobe ($B = 0$). (c),(d) Same as (a),(b) except in the first lobe ($B = 104$ mT). Higher frequency oscillations in first lobe (d) reflects higher effective drive power than in (b).

one cannot place an experimental bound on E_M away from zero.

We next examine charge dispersion in the two lobes in device 2. The fine-scale dependence of the qubit transition frequency on gate voltage V_C, swept over a small range, is shown in Fig. 4(a). The interlaced sinusoidal qubit response as a function of V_C (column average subtracted) represents the two charge parity branches, visible in the offset-charge-sensitive regime, as investigated previously in conventional [31] and semiconducting junctions [12,13]. The simultaneous visibility of both parity branches indicates parity switching (poisoning) that is fast compared to the measurement time [31].

Coherent qubit oscillations in both parity branches in the zeroth lobe ($B = 0$) are shown in Fig. 4(b) [qubit response $V_H(\tau = 0)$ subtracted from all columns for better visibility] and are measured at a more positive V_C, which increased the qubit frequency and slightly reduced dispersion. Rabi oscillations as a function of qubit drive time τ and drive frequency, f_d, are similar in the two parity branches. Comparable measurements in the first lobe ($B = 104$ mT), are shown in Figs. 4(c) and 4(d). We note that data in Figs. 4(b) and 4(d) were measured at V_C values producing the largest frequency difference between the two parity branches at that particular qubit frequency. The slow drift

that is visible in Fig. 4(c) is related to a small change in the junction conductance, which only changes considerably over a larger scale of V_C. Overall, no clear splitting at the parity crossing can be resolved here in Fig. 4(c) or in a broader range of gate voltages. We are able to place an upper bound, $E_M/h < 10$ MHz [38] based on the absence of a well-resolved splitting. We do not know if the absence of resolvable splitting of the parity branches reflects an absence of zero-energy states (due to the lack of tunability of material parameters), their negligible coupling across the junction (due to the sensitivity to electrostatic environment), or a short coherence due to rapid poisoning [6,7,32] from other low energy subgap states in the first lobe.

*These authors contributed equally to this work.

[1] J. Koch, T. M. Yu, J. Gambetta, A. A. Houck, D. I. Schuster, J. Majer, A. Blais, M. H. Devoret, S. M. Girvin, and R. J. Schoelkopf, Phys. Rev. A **76**, 042319 (2007).

[2] M. H. Devoret and R. J. Schoelkopf, Science **339**, 1169 (2013).

[3] G. de Lange, B. van Heck, A. Bruno, D. J. van Woerkom, A. Geresdi, S. R. Plissard, E. P. A. M. Bakkers, A. R. Akhmerov, and L. DiCarlo, Phys. Rev. Lett. **115**, 127002 (2015).

[4] T. W. Larsen, K. D. Petersson, F. Kuemmeth, T. S. Jespersen, P. Krogstrup, J. Nygård, and C. M. Marcus, Phys. Rev. Lett. **115**, 127001 (2015).

[5] L. Casparis, T. W. Larsen, M. S. Olsen, F. Kuemmeth, P. Krogstrup, J. Nygård, K. D. Petersson, and C. M. Marcus, Phys. Rev. Lett. **116**, 150505 (2016).

[6] M. Hays, G. de Lange, K. Serniak, D. J. van Woerkom, D. Bouman, P. Krogstrup, J. Nygård, A. Geresdi, and M. H. Devoret, Phys. Rev. Lett. **121**, 047001 (2018).

[7] F. Luthi, T. Stavenga, O. W. Enzing, A. Bruno, C. Dickel, N. K. Langford, M. A. Rol, T. S. Jespersen, J. Nygård, P. Krogstrup, and L. DiCarlo, Phys. Rev. Lett. **120**, 100502 (2018).

[8] L. Casparis, N. J. Pearson, A. Kringhøj, T. W. Larsen, F. Kuemmeth, J. Nygård, P. Krogstrup, K. D. Petersson, and C. M. Marcus, Phys. Rev. B **99**, 085434 (2019).

[9] A. Kringhøj, T. W. Larsen, B. van Heck, D. Sabonis, O. Erlandsson, I. Petkovic, D. I. Pikulin, P. Krogstrup, K. D. Petersson, and C. M. Marcus, Phys. Rev. Lett. **124**, 056801 (2020).

[10] L. Tosi, C. Metzger, M. F. Goffman, C. Urbina, H. Pothier, S. Park, A. L. Yeyati, J. Nygård, and P. Krogstrup, Phys. Rev. X **9**, 011010 (2019).

[11] A. Kringhøj, L. Casparis, M. Hell, T. W. Larsen, F. Kuemmeth, M. Leijnse, K. Flensberg, P. Krogstrup, J. Nygård, K. D. Petersson, and C. M. Marcus, Phys. Rev. B **97**, 060508(R) (2018).

[12] A. Bargerbos, W. Uilhoorn, C.-K. Yang, P. Krogstrup, L. P. Kouwenhoven, G. de Lange, B. van Heck, and A. Kou, Phys. Rev. Lett. **124**, 246802 (2020).

[13] A. Kringhøj, B. van Heck, T. W. Larsen, O. Erlandsson, D. Sabonis, P. Krogstrup, L. Casparis, K. D. Petersson, and C. M. Marcus, Phys. Rev. Lett. **124**, 246803 (2020).

[14] M. Hays, V. Fatemi, K. Serniak, D. Bouman, S. Diamond, G. de Lange, P. Krogstrup, J. Nygrd, A. Geresdi, and M. H. Devoret, Nat. Physics (2020) https://doi.org/10.1038/s41567-020-0952-3.

[15] T. W. Larsen, M. E. Gershenson, L. Casparis, A. Kringhøj, N. J. Pearson, R. P. G. McNeil, F. Kuemmeth, P. Krogstrup, K. D. Petersson, and C. M. Marcus, Phys. Rev. Lett. **125**, 056801 (2020).

[16] W. A. Little and R. D. Parks, Phys. Rev. Lett. **9**, 9 (1962).

[17] Y. Liu, Y. Zadorozhny, M. M. Rosario, B. Y. Rock, P. T. Carrigan, and H. Wang, Science **294**, 2332 (2001).

[18] I. Sternfeld, E. Levy, M. Eshkol, A. Tsukernik, M. Karpovski, H. Shtrikman, A. Kretinin, and A. Palevski, Phys. Rev. Lett. **107**, 037001 (2011).

[19] S. Vaitiekėnas, P. Krogstrup, and C. M. Marcus, Phys. Rev. B **101**, 060507(R) (2020).

[20] S. Vaitiekėnas, G. W. Winkler, B. van Heck, T. Karzig, M.-T. Deng, K. Flensberg, L. I. Glazman, C. Nayak, P. Krogstrup, R. M. Lutchyn, and C. M. Marcus, Science **367**, eaav3392 (2020).

[21] F. Hassler, A. R. Akhmerov, and C. W. J. Beenakker, New J. Phys. **13**, 095004 (2011).

[22] T. Hyart, B. van Heck, I. C. Fulga, M. Burrello, A. R. Akhmerov, and C. W. J. Beenakker, Phys. Rev. B **88**, 035121 (2013).

[23] E. Ginossar and E. Grosfeld, Nat. Commun. **5**, 4772 (2014).

[24] C. Ohm and F. Hassler, Phys. Rev. B **91**, 085406 (2015).

[25] J. Avila, E. Prada, P. San-Jose, and R. Aguado, Phys. Rev. Research **2**, 033493 (2020).

[26] R. M. Lutchyn, E. P. A. M. Bakkers, L. P. Kouwenhoven, P. Krogstrup, C. M. Marcus, and Y. Oreg, Nat. Rev. Mater. **3**, 52 (2018).

[27] J. G. Kroll, F. Borsoi, K. L. van der Enden, W. Uilhoorn, D. de Jong, M. Quintero-Pérez, D. J. van Woerkom, A. Bruno, S. R. Plissard, D. Car, E. P. A. M. Bakkers, M. C. Cassidy, and L. P. Kouwenhoven, Phys. Rev. Applied **11**, 064053 (2019).

[28] D. M. T. van Zanten, D. Sabonis, J. Suter, J. I. Vyrynen, T. Karzig, D. I. Pikulin, E. C. T. OFarrell, D. Razmadze, K. D. Petersson, P. Krogstrup, and C. M. Marcus, Nat. Phys. **16**, 663 (2020).

[29] J. Avila, E. Prada, P. San-Jose, and R. Aguado, Phys. Rev. B **102**, 094518 (2020).

[30] A. Keselman, C. Murthy, B. van Heck, and B. Bauer, SciPost Phys. **7**, 50 (2019).

[31] J. A. Schreier, A. A. Houck, J. Koch, D. I. Schuster, B. R. Johnson, J. M. Chow, J. M. Gambetta, J. Majer, L. Frunzio, M. H. Devoret, S. M. Girvin, and R. J. Schoelkopf, Phys. Rev. B **77**, 180502(R) (2008).

[32] K. Serniak, M. Hays, G. de Lange, S. Diamond, S. Shankar, L. D. Burkhart, L. Frunzio, M. Houzet, and M. H. Devoret, Phys. Rev. Lett. **121**, 157701 (2018).

[33] K. Serniak, S. Diamond, M. Hays, V. Fatemi, S. Shankar, L. Frunzio, R. J. Schoelkopf, and M. Devoret, Phys. Rev. Applied **12**, 014052 (2019).

[34] D. Rist, C. C. Bultink, M. J. Tiggelman, R. N. Schouten, K. W. Lehnert, and L. DiCarlo, Nat. Commun. **4**, 1913 (2013).

[35] V. H. Dao and L. F. Chibotaru, Phys. Rev. B **79**, 134524 (2009).

[36] In detail, the following implicit equation need to be solved for Δ given α: $\ln(\Delta_0/\Delta) = \pi\alpha/4\Delta$ for $\alpha > \Delta$ and $\ln(\Delta_0/\Delta) = \ln[\alpha + (\alpha^2 - \Delta^2)^{1/2}/\Delta] - [(\alpha^2 - \Delta^2)^{1/2}/2\alpha] + (\alpha/2\Delta)\arcsin(\Delta/\alpha)$ for $\alpha < \Delta$. This expression appears as Eq. (26) in Ref. [37].

[37] A. I. Larkin, JETP **21**, 153 (1965), http://www.jetp.ac.ru/cgi-bin/dn/e_021_01_0153.pdf.

[38] The numerical code and data accompanying the analysis can be found at https://doi.org/10.5281/zenodo.3779035.

[39] 'See the Supplemental Material at http://link.aps.org/supplemental/10.1103/PhysRevLett.125.156804 for an exemplary magnetic field dependence of qubit lifetime in device 1.